Journal of Materials Chemistry C

Accepted Manuscript

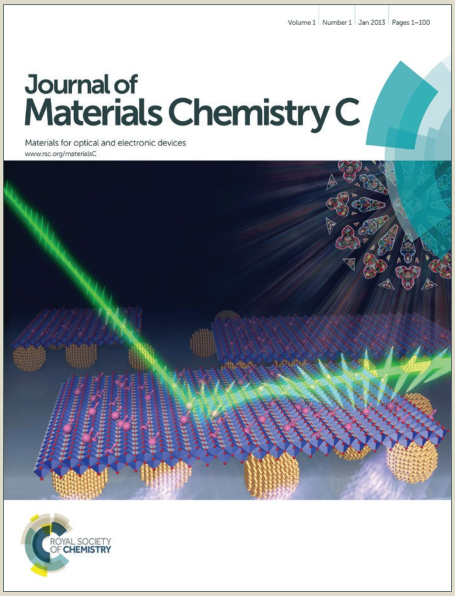

ROYAL SOCIETY OF CHEMISTRY

www.rsc.org/materialsC

Highly Conductive, Optically Transparent, Low Work-Function Hydrogen-doped Boron-doped ZnO Electrodes for Efficient ITO-Free Polymer Solar Cells

Ermioni Polydorou[1,2], Anastasia Soultati[1,3] and Maria Vasilopoulou[1,*]

[1]*Institute of Nanoscience and Nanotechnology, National Center for Scientific Research Demokritos, 15310, AghiaParaskevi, Attiki, Greece*

[2]*Department of Physics, University of Patras, 26504 Patras, Greece*

[3]*Department of Chemical Engineering, National Technical University of Athens, 15780 Athens, Greece*

**email: m.vasilopoulou@inn.demokritos.gr*

Abstract

In this work, highly conductive, optically transparent and low work-function hydrogen-doped boron-doped ZnO (BZO:H) cathode electrodes were prepared by a hydrogen post annealing treatment of the as-deposited boron-doped ZnO (BZO) samples. It was found that hydrogen post annealing at temperatures around 200 °C resulted in the formation of electrode materials which exhibited higher conductivity and carrier concentration, reduced sheet resistance and significantly increased optical transparency when compared with their non-annealed BZO counterparts. In addition, hydrogen incorporation in these materials' lattice caused a significant reduction in their work function which may be beneficial for device operation. As a result, polymer solar cells using BZO:H films as transparent cathode electrodes exhibited higher efficiencies from those obtained in devices using the non-annealed counterparts. In particular, devices based on the poly(3-hexylthiophene) (P3HT):[6,6]-phenyl C71butyric acid methyl ester ($PC_{71}BM$) system as the photoactive layer exhibited a PCE of 3.90%, whereas those based on the poly[(9-(1-octylnonyl)-9H-carbazole-2,7-diyl)-2,5-thiophenediyl-2,1,3-benzothiadiazole-4,7-diyl-2,5-thiophenediyl] (PCDTBT):$PC_{71}BM$ and poly[[4,8-bis[(2-ethylhexyl)oxy]benzo[1,2-b:4,5-b']dithiophene-2,6-diyl][3-fluoro-2-[(2-ethylhexyl) carbonyl]thieno[3,4-b]thiophenediyl]] (PTB7:$PC_{71}BM$) as the active components reached high PCE values

of 5.90 % and 7.25 % respectively, which are comparable or even higher from reported efficiencies obtained in devices using doped ZnO-based transparent electrodes.

1. Introduction

Growing concerns about global warming demands the expansion of renewable energy sources as viable alternatives to fossil-fuel-based technologies. This could explain the increasing amount of research devoted to new types of solar energy conversion devices, such as those based on semiconducting polymers, which fall into the category of polymer solar cells (PSCs).[1-4] To date, organic solar cells based on interpenetrating networks of low bandgap electron-donors and fullerene acceptors have exhibited power conversion efficiencies (PCEs) exceeding 9% for single-junction PSCs[5-8] and 11% for tandem-junction cells consisting of stacks of individual cells with complementary absorption.[9-12] However, to promote the PSCs in the viable applications, further enhancements in the efficiency are urgently required. Besides the design and synthesis of low-bandgap polymer materials with higher absorption efficiency and charge mobilities,[13,14] and/or the interface modification by using suitable interfacial layers for efficient charge collection by the electrodes[15-18] replacing the conventional indium tin oxide (ITO) and fluorinated tin oxide (FTO) with alternative transparent conducting electrodes remains one of the major challenges for single-junction and tandem PSCs. These electrode materials should be highly conductive and optically transparent; meanwhile, they should also be low cost and enable new attractive features.

Transparent conducting oxide (TCO) films have been extensively applied to optoelectronic devices,[18] chemical sensors,[19] and solar cells.[20] Doped zinc oxide (ZnO) thin films, in particular, have been investigated as promising transparent conducting layers for photovoltaic devices as an alternative to indium tin oxide thin films because the impurity doping significantly improves the electrical and optical properties of these films.[21] The group III elements, such as boron (B),[22] aluminum (Al),[23] gallium (Ga),[24] and indium (In)[25] have been intensively investigated for the doping of ZnO. It was demonstrated that the group III elements could work as n-type dopants for ZnO to replace Zn sites and generate free electrons.[26] Because the indium element in ITO films is comparatively rare, the doped ZnO films have been investigated as an alternative to ITO for their excellent compromise on electrical and optical properties, low price, abundance of raw materials and simplicity of fabricating process.[27-30] Due to their obvious benefits, ZnO-based TCO films have been introduced into inverted polymer solar cells as either charge transport interfacial layers[31-41] or bottom electrode materials.[42-49] Among the various doping methods, aluminum and gallium doping are well-known approaches to enhance the conductivity of ZnO layers for use as bottom electrodes in inverted PSCs.[44-49] To nowadays, well-performing inverted PSCs based on Al or Ga doped bottom electrodes with modified crystallinities and optical properties have been demonstrated. However, up to now the successful application of boron doped ZnO (BZO) layers as transparent electrodes in PSCs has not been demonstrated.

In this work, we report on the electrical, optical and structural/electronic properties of boron-doped ZnO (termed hereafter as BZO) thin films before and after hydrogen post annealing for use as bottom cathode electrodes in inverted PSCs. It was found that hydrogen annealing at temperatures around 200 ^{o}C (and above) resulted in the formation of hydrogen-doped BZO electrodes (termed hereafter as BZO:H) which exhibited significantly improved conductivity, carrier concentration, Hall mobility and optical transparency whereas they also presented reduced work function value when compared with their non-annealed counterparts. As a result, PSC devices using BZO:H films as cathode electrodes and the well-known poly(3-hexylthiophene) (P3HT):[6,6]-phenyl C71butyric acid methyl ester ($PC_{71}BM$) system as the photoactive layer exhibited a power conversion efficiency (PCE) of 3.9% which was 20% improved relative to that exhibited by the reference device with the conventional FTO cathode (PCE=3.30%) whereas these devices also exhibited exceptional environmental stability. In addition, by using poly[(9-(1-octylnonyl)-9H-carbazole-2,7-diyl)-2,5-thiophenediyl-2,1,3-benzothiadiazole-4,7-diyl-2,5-thiophenediyl] (PCDTBT):$PC_{71}BM$ or poly[[4,8-bis[(2-ethylhexyl)oxy]benzo[1,2-b:4,5-b']dithiophene-2,6-diyl][3-fluoro-2-[(2-ethylhexyl) carbonyl]thieno[3,4-b]thiophenediyl]] (PTB7:$PC_{71}BM$) as the active component in the solar cell a high PCE of 5.90 % or 7.25%, respectively, was achieved, which were higher than those of the reference devices using either the non-annealed BZO or FTO cathodes. Based on these results, we believe that our prescription for the control of optical and electronic properties of ZnO-based electrode materials using a hydrogen post-annealing treatment, constitute a step forward in the engineering of electrode materials which is a necessary achievement for the selection of the most suited properties to be exploited not only to PSCs but also in the different kinds of optoelectronic applications.

2. Experimental details

Synthesis of BZO and BZO:H films. BZO films -100 nm thick- were fabricated on glass substrates using Metal-Organic Chemical Vapor Deposition (MOCVD). Diethylzinc and H_2O vapor were used as the precursors with flow rates of 180 sccm and 110 sccm, respectively. In addition, diborane was used as a doping gas. The growth temperature was kept at approximately 150 ^oC, and the pressure in the deposition reactor was 0.02 Torr. The B doping ratio of BZO films was change by adjusting the flow rate of diborane with respect to the flow rates of the precursor gases. Next, BZO films were hydrogen doped (to formulate BZO:H films) by annealing at elevated temperatures in a pure hydrogen environment.

Device Fabrication. PSC devices were fabricated on TCO coated glass substrates. The FTO/glass substrates with a mean thickness of 100 nm, a sheet resistance of ~13 Ω/sq and a transmittance of 82-84.5% in the visible wavelength region were purchased from Sigma-Aldrich and served as the cathode electrodes in the reference devices. The BZO and BZO:H electrodes were deposited on glass substrates identical as those of FTO films. Prior to deposition glass substrates were ultrasonically cleaned with a standard solvent regiment (15 min each in acetone and isopropanol). Next, a ZnO layer with a thickness of approximately 40 nm was deposited, following a sol-gel method,[50,51] to serve as the electron transport layer followed by an approximately 100 nm photoactive layer. The active layer was consisting of P3HT:$PC_{71}BM$ blend (1:0.8 wt% ratio) or PCDTBT:$PC_{71}BM$ (1:4 wt% ratio) and it was spin-cast on top of the ZnO film from a 20 mg mL^{-1} chlorobenzene solution. After being spin- coated, the active layer was annealed at 140 °C (P3HT:$PC_{71}BM$) or at 70 ^oC (PCDTBT:$PC_{71}BM$) for 10 min in air. In the case of PTB7:PC71BM (10 mg ml^{-1} for PTB7, 15 mg ml^{-1} for $PC_{71}BM$ blend in chlorobenzene) a 3% per volume of DIO was added in the solution). After spin coating, the photoactive layer was annealed either at at 70 °C for 20 min in air. Then, an approximately 20 nm-thick under-stoichiometric molybdenum oxide (MoO_x) layer was deposited on top of the active layer, using the previously reported hot-wire deposition method,[34,35] to serve as the hole extraction layer. The devices were completed with a 150 nm thick aluminum anode, deposited in a dedicated thermal evaporator at a pressure of 10^{-6} Torr through a shadow-mask, which defined the device active area to be equal to 12.56 mm^2. The devices were then measured in air at room temperature without additional encapsulation. All chemicals were purchased from Sigma-Aldrich and used with no further purification.

Characterization. The valence band spectra of different TCO and ZnO films were evaluated after recording the ultraviolet photoelectron spectroscopy (UPS) spectra. For the UPS measurements, the He I (21.22 eV) excitation line was used. A negative bias of 12.28 V was applied to the samples during UPS measurements in order to separate sample and analyzer high binding energy (BE) cut-offs and estimate the absolute work function value from the high BE cut-off region of the UPS spectra. ZnO-based TCO film surface elemental analysis was performed on a Perkin-Elmer Φ 5600ci X-ray photoelectron spectrometer, using a nonmonochromatized MgKα excitation source (1253.6 eV). The binding energy shifts were corrected assigning to the C1s line of adventitious carbon a value of 284.8 eV. To validate the luminescence properties for BZO and BZO:H films, photoluminescence (PL) spectroscopy was performed at room temperature using a 325 nm He-Cd laser line. Time-resolved photoluminescence (TRPL) spectroscopy was also conducted using a mode-locked Ti:Sapphire layer (Chameleon Ultra II, Coherent Inc.) operating at 350 nm with a 150 fs pulse duration and a repetition rate of 80 MHz, with the 2nd harmonic produced by β-BaBO4 crystal in order to clearly elucidate the recombination dynamics from the observed emission features in these films. Film thickness was estimated with ellipsometry. EQE measurements were carried out using an Autolab PGSTAT-30 potentiostat, with a 300 W Xe lamp in combination with an Oriel 1/8 monochromator for dispersing the light in an area of 0.5 cm2. A Thorlabs silicon photodiode was used for the calibration of the spectra. The structural characterization of the samples was carried out by wide angle X-ray diffraction (reflection mode) using a Bruker D8 Discover diffractometer with Ni-filtered Cu-Kα radiation source (λ=1.5406 ˚A) equipped with a LynxEye position sensitive detector. The surface morphology was probed with scanning electron microscopy (SEM) measurements using a FEI Inspect instrument equipped with Genesis Spectrum v.4.52 software for X-ray microanalysis (EDAX). The capacitance-voltage measurements were recorded on devices exhibiting the same architecture as described above (OPVs) at a frequency of 100 KHz and an AC bias of 25 mV by using a Keithley 4200–SCS DC characterization system. The measurements were performed in air at room temperature. Absorption and transmittance measurements were taken using a Perkin Elmer Lampda 40 UV/Vis spectrophotometer. Current density-voltage characteristics of the fabricated solar cells were measured with a Keithley 2400 source-measure unit. Cells were illuminated with a Xe lamp and an AM 1.5G filter to simulate solar light illumination conditions with an intensity of 100 mW/cm^2 (1 sun), as was recorded with a calibrated silicon photodiode. To accurately define the active area of all devices we used aperture masks during the measurements with their area equal to those of the Al contacts (12.56 mm^2).

3. Results and discussion

The electrical properties of the as-deposited boron-doped ZnO (BZO) films for various B contents are shown in Figures 1a and 1b. Overall, significant changes were observed for electrical parameters such as electrical resistivity and carrier concentration (Figure 1a), Hall mobility and sheet resistance (Figure 1b) when B doping was increased from 0% up to about 3%. The resistivity of BZO film decreased from 3.0×10^{-3} to 2.4×10^{-4} Ω cm with the increase of B content from 0 to 2%, due to both, the increase of carrier concentration from 1.74 x10^{17} cm^{-3} to 3.02 x10^{20} cm^{-3} (which indicates that part of the incorporated B atoms act as donors and provide free carriers to the ZnO) and Hall mobility from 3.6 cm^2 V^{-1} s^{-1} to 38.0 cm^2 V^{-1} s^{-1}, respectively. With the increase of B doping up to about 3%, the resistivity of BZO films slightly increased while the carrier concentration and Hall mobility were decreased. However, it is hard to interpret that the amount of such variation is meaningful. Additionally, there is a large decrease in the sheet resistance of the BZO film as the B content increases from 0 to 2% (from 65 Ω/sq to 20 Ω/sq); note that reduced sheet resistance is a prerequisite for using these films as electrode materials. From the above results becomes evident that an amount of about 2% of B content in BZO films is sufficient to obtain adequate electronic properties of these films. However, further enhancement of those properties was achieved after annealing in hydrogen environment at elevated temperatures, as shown in Figures 1c and 1d. When annealed in hydrogen at temperatures from 0 to 200 ^{o}C (the duration of annealing was kept constant at 30 min) the BZO films exhibited further significant decrease in resistivity and sheet resistance reaching values of 1.5×10^{-4} Ω cm and 10 Ω/sq whereas their carrier concentration and Hall mobility were increased to 5.25x10^{20} cm^{-3} and 58.4 cm^2 V^{-1} s^{-1}, respectively. This increase in carrier concentration and Hall mobility can be due to the incorporation of hydrogen donor in ZnO crystal. However, one should argue that at high substrate temperatures oxygen might be desorbed or removed by reaction with hydrogen, forming oxygen vacancies and decreasing the resistivity of BZO although this is not expected to be observed at relatively low temperatures. However, since the resistivity of BZO film is starting to decrease with increasing the substrate temperature just above the room temperature during annealing, the formation of oxygen vacancies should not be the major (or at least the only) mechanism in enhancing the conductivity of BZO:H films. This is also supported by the small reduction in carrier concentration and Hall mobility (followed by an increase in resistivity and sheet resistance) at temperatures above 200 ^{o}C. Therefore, our results indicate that hydrogen donor is responsible for the increase of carrier concentration in BZO, as theoretically suggested by Van de Walle,[52,53] and experimentally confirmed by S. Cox et al.[54]

In Figure 2a the steady-state PL spectra of the BZO (with 2% B content) and BZO:H films (formed by annealing the BZO films in H_2 at 200 ^{o}C) samples, are shown. It is apparent that the spectra of the non-annealed B-doped samples, except of the band-to-band sharp UV emission peak, are dominated by a broad emission in the visible wavelength region, while the scan for the annealed H-doped BZO sample is only governed by the band-to-band emission. The time-resolved PL spectral plot used to determine exciton lifetimes is given in Figure 2b. As evident in the figure, the B-doped exhibits fast decay times of 80.8 ps. According to previous reports on undoped ZnO thin films, a fast recombination time of less than 74 ps is associated with the non-radiative recombination of non-radiative defects in ZnO, including vacancy complexes that include Zn vacancies.[55,56] Therefore, as-grown B-doped ZnO films displaying similarly short lifetimes are more likely to maintain non-radiative recombination centers with pristine ZnO films. However, the hydrogen annealed B-doped ZnO film exhibits radiative recombination lifetimes (as determined by fitting bi-exponential decay curves) of 102 ps and 922 ps. The suppressed visible emission of the steady-state PL spectra and the longer lifetime of the H-doped B-doped ZnO films reflect a reduction in defects that serve as carrier traps. This is an additional advantage of these materials when used as electrode materials in optoelectronic applications. UV–visible spectroscopy was also employed to measure the optical transmittance of BZO films, as-deposited and after hydrogen annealing at 200 ^{o}C. As shown in Figure 2c, the transmittance of the as-grown BZO film fell off steeply with decreasing wavelength around 380 nm, which is a characteristic of high quality ZnO-based films. The BZO films exhibit adequate transparency with the transmittance to vary between 82% and 85.6% in the visible wavelength region. However, when H_2 is inserted inside the material's lattice, the transmittance is significantly increased and varies between 88% and

96%. Note that, the reduced transmittance of both films in the near infrared region is attributed to absorption and reflection by free carriers. In addition, the transmittance edge shifts to a lower wavelength. The phenomenon might be due to the Burstein–Moss effect,[57] pointing out that the Fermi level inside the conduction band moves upward with increasing donor concentration due to the filling of conduction band by the increase of electron carriersand, consequently, electrons can no longer be excited from the valence band maximum to the minimum of the conduction band. Instead higher energies are needed to reach unoccupied states. This so-called Pauli blocking leads to an increase of the optical band gap (Figure 2d).The increase of carrier concentrations in the BZO:H films is thus concluded from as measured UV–visible spectroscopy in consistency with the electrical properties by electrical measurements. From the above analysis it is deduced that the electrical and optical properties of hydrogen-annealed BZO films were significantly improved in comparison with the non-annealed counterparts.

To probe possible structural differences between the BZO and BZO:H films their X-ray diffraction **(**XRD) patterns were obtained and are presented in Figures 3a and 3b, respectively. It is seen that both XRD patterns exhibit a small peak at 31^{o} attributed to (100) plane and a large peak around 34° attributed to (002) plane. This result suggests that these films are consisting of crystallites with preferred orientation along the c axis. With annealing in hydrogen the (002) peak increases in intensity and also is shifted to a higher 2θ value (from 33.78 to 34.20^{o}), indicating a decrease of interplanar distance. The mean values of grain size R of the BZO-based films were evaluated from the full-width at half-maximum (FWHM) of the (002) peak using the Scherrer's formula,[58] and found 26.1 nm and 27.2 nm for BZO and BZO:H films, respectively. The increase in R with annealing in hydrogen confirms the improved crystalline quality of the BZO:H films. This trend is in agreement with the result derived from SEM surface images presented in Figures 3c and 3d for BZO and BZO:H films, respectively. It is obvious that both films showed a pyramid-like morphology which was remained nearly unaffected by the hydrogen annealing treatment. The BZO films exhibited slightly more dense morphology and smaller surface grain size when compared with the BZO:H ones, in agreement with the XRD results. Moreover, from XRD patterns the crystalline plane distance (lattice parameter), d, was also calculated from the Bragg diffraction equation: $\lambda=2d\sin\theta$, where λ is the X-ray wavelength (1.54 Å) and θ is the diffraction angle of the (002) peak. In particular, the lattice parameter d in the BZO film is about 2.611A˚, and the d value of hydrogen-annealed BZO:H film is 2.603A˚.

The texture coefficient for the (002) orientation was estimated from the following equation:[59]

$$TC_{(002)} = \frac{I_{(002)} / I^{0}_{(002)}}{(1/N)\sum_{n} I_{(hkl)} / I^{0}_{(hkl)}} \qquad (1)$$

where $TC_{(002)}$ is the texture coefficient of the (002) plane, I(hkl), I(002) are the measured intensities of the (hkl) and (002) peaks, respectively, I^0(hkl) and I^0(002) are the recorded intensities on a completely random sample taken from a powder diffraction file card; and N is the number of diffractions considered in the analysis. A sample with randomly oriented crystallite yields TC(hkl)=1, while the larger this value, the larger abundance of crystallites oriented at the (hkl) direction. The calculated texture coefficients TC (002) are 3.7 and 4.1 for BZO and BZO:H films, respectively. It can be seen that the highest TC is obtained for the (002) plane of the BZO:H thin film. The higher value of texture coefficient reveals that the zinc oxide film crystallinity is improved.

Next, in order to investigate the chemical states of elements in the BZO-based films for clarifying mechanisms for the improvement in resistivity, XPS measurements were performed. In the beginning of the XPS measurements, the binding energy of the photoelectron was calibrated by assigning 284.8 eV to the C1s peak corresponding to adventitious carbon. Figures 4a, 4b, 4c show the core level peaks of the XPS spectra of Zn 2p, of B 1s and O 1s, respectively, taken in BZO and BZO:H films. The core level peaks of binding energies of Zn $2p_{1/2}$ and $2p_{3/2}$ for zinc ions are located at 1044.1 and 1022.0 eV, respectively, in the as-deposited BZO film. The intensities and area ratios of Zn 2p components exhibit no changes after hydrogen annealing (Figure 4a). However, the component peaks are slightly shifted toward the higher energy side in the hydrogenated film, revealing possible formation of Zn-H bonds in that film.[60] The binding energy peak located at approximately 192.1 eV is associated with the B^{3+} in B_2O_3 structure (Figure 4b), which provides the evidence for the incorporation of boron into the zinc oxide.[61] The intensities and area ratios of this peak remains quite similar for both films which is an indication that boron content is not affected by hydrogen annealing. Figure 4c shows the O 1s XPS spectrum of the BZO and BZO:H films. The profile of the O 1s spectrum was fitted using the Lorentzian–Gaussian functions. The binding energy peaks located at 530.0 and

531.1 eV are attributed to lattice oxygen (Zn-O bonds) and hydroxyl ions (Zn-OH), respectively.[62] The presence of hydrogen atoms (in the form of –OH anions bonded to Zn cations) is evident in the case of the hydrogen annealed sample which is a strong indication of hydrogenation of this sample during annealing. This result suggests that the incorporation of H impurities may play the key role in the improvement in current conduction in the amorphous BZO:H films.

Next, in order to explore the electronic properties of the BZO-based samples ultraviolet photoelectron spectroscopy (UPS) measurements were performed. In Figures 4d and 4e the secondary electron cut-off and the valence band spectra of BZO and BZO:H films are shown. Note that, for comparison reasons, the spectrum of an FTO film with the same thickness in also included in these Figures. FTO and BZO films possess a W_F of 4.7 eV and 4.4 eV, respectively, while BZO:H shows significantly reduced W_F with decreased value of 0.3eV. The most widely used theory to explain the W_F decreasing phenomenon is the formation of an interfacial dipole when the materials interact (through adsorption, chemisorption or other) with electron-donating elements, such as hydrogen. In our case, during hydrogen annealing, H atoms may are bonded to oxygen atoms present on the surface of BZO forming hydroxyl groups as evidenced by the XPS measurements and also by FTIR transmittance spectra (Figure S1) taken on BZO and H_2 annealed-BZO films. As a strong electron-donating compound, H atom could form strong interfacial dipole on ZnO surface when it is bonded to oxygen atom on the surface of Zn-O lattice, resulting in a decrease of the hydrogen treated oxide's surface work function relative to its non-treated counterpart, as shown in Figure 4d. The above data indicate an additional benefit of BZO:H for use as the low-work function cathode electrode contact in PSC devices.

We next investigated the effect of incorporating the BZO films described previously as bottom cathode electrodes in bulk-heterojunction (BHJ) PSCs based on different donors, such as the well-known P3HT, and the recently introduced small band gap donors PCDTBT and PTB7, and the $PC_{71}BM$ acceptor. The device structure was glass/BZO or BZO:H or FTO (bottom cathode electrode)/ZnO (40 nm) (electron extraction layer)/active layer/MoO_x (20 nm)(hole extraction layer)/Al (top anode electrode). Shown in Figure 5a are the device architecture and the chemical structures of organic semiconductors used in this study. Noting that, the electron extracting ZnO layer was fabricated using a solution based sol-gel method which resulted in the formation of a ZnO film consisting of nanoparticles with a rod-like morphology (Figure S2) and exhibiting a surface roughness of 4.9 nm. Several ZnO film thicknesses were evaluated (not shown) with the thickness of 40 nm delivering the highest device efficiency which was attributed to uniform coverage and smoothening of the rough surface of bottom electrodes. The UPS spectrum and Tauc plot (as derived from absorption measurements) of these films are also shown in Figure S3 and were used for the estimation of their energy levels. In Figure S4 the UPS spectrum and Tauc plot of a MoO_x film which was used as the hole extraction layer, are also shown. The selection of MoO_x as anode buffer layer was due to its well established hole extracting capabilities in order to enhance the efficiency of hole harvesting at the anode. The electronic structure of this oxide was previously investigated, and was found to be a very high work function n-type oxide, doped by oxygen vacancies.[63,64] According to UPS and absorption measurements the energy level alignment (before contact) of materials used at the different layers in our devices are shown in Figures 5b and 5c in the cases of FTO and BZO:H bottom cathode electrodes, respectively. It is obvious that in the case of FTO cathode a large electron extraction barrier between this electrode and ZnO buffer layer of about 0.6 eV can be concluded which may deteriorate the device performance. However, this is not the case for the BZO:H/ZnO interface where a nearly barrier free electron extraction is derived from the energy level alignment presented in Figure 5c. Taking into account that the Fermi level of ZnO is expected to be pinned with the LUMO of $PC_{71}BM$,[65] Ohmic electron extracting cathode interfaces may be formed when using the BZO:H electrode. Indeed, such a speculation is confirmed by the current density-voltage (J-V) characteristics taken under simulated 1.5 AM solar illumination in our devices and shown in Figures 6a for the case of P3HT:$PC_{71}BM$ active layer (PSC 1) (Table 1 also summarizes the devices operational characteristics). From the J-V curves becomes evident that devices based on the same active layer and different BZO anode electrodes show significant improvement in their short-circuit current (J_{sc}) and open-circuit voltage (V_{oc}) when using the hydrogenated BZO:H as transparent cathodes. For PSC 1 (Figure 6a), the device with the BZO electrode exhibits a PCE of 2.80% whereas the one with the BZO:H electrode shows a PCE of 3.90% (which represents a 40% improvement) whereas the PCE value obtained in the reference device with the FTO cathode is 3.30%. Noting that, the value PCE of 3.90% is also higher from the value of 3.01% which was obtained in previously reported P3HT:$PC_{71}BM$ based inverted PSCs using aluminum-doped zinc oxide cathode and low-temperature aqueous solution processed zinc oxide electron extraction layer.[42] The efficiency enhancement is a direct result of improved J_{sc} and also V_{oc} and fill factor (FF) in the BZO:H incorporating device compared with the BZO and FTO-based ones. The enhancement of J_{sc} and also in FF are reflected in the considerable reduction of the series resistance, R_s, of BZO:H based devices as evidenced from the increased slopes in the dark current measurements of the diodes based on P3HT:PC_{71}BM (Figure 6b). Reduced R_s suggests improved contact between the active layers and cathode, which facilitates free charge-carrier extraction and therefore enhanced J_{sc} and FF in the devices with the hydrogen-annealed BZO electrodes as compared with the ones using the BZO or FTO cathodes. In addition, high external quantum efficiency (EQE) values were observed in the devices using the BZO:H cathode (Figures 6c). This enhancement in EQEs suggests that the photon-to-electron conversion processes are very efficient in these devices. The improved EQE spectra provide clear evidence for the enhanced charge generation/extraction and suggest that charge separation and carrier extraction are significantly enhanced, thus resulting in an increase of the device photocurrent and can be attributed to higher transparency of the hydrogenated BZO cathodes. Note that the significant enhancement in the absorption of P3HT:PC_{71}BM film when deposited on top of the BZO:H layer (Figure S5a) may explain the increase of EQE. Such enhancement is derived from the increased transparency of the specific electrode material and not from improved film nanomorphology (Figure S5b).

To further demonstrate that the improved quality of cathode electrodes is the main reason for the improved performance obtained in the devices using the hydrogenated BZO:H electrodes as compared with the devices using the BZO ones, we fabricated electron-only devices (with the structure BZO or BZO:H or FTO/ZnO (40 nm) /P3HT:PC_{71}BM (100 nm)/Al) and measure their J-V characteristics, which are shown in Figure 6d. The hole current in these devices is completely suppressed by subtracting the MoO_x interlayer from the top contact. It is observed that the currents density in the devices can be manipulated within a range of about two orders of magnitude by changing the BZO electrode to FTO and, especially, to BZO:H ones. We have analyzed our electron-only devices using a space-charge-limited current (SCLC) model to fit the experimental results using analogues of Child's Law,[66] which describes single carrier currents in a trap-free insulator and predicts that the current density (J) varies by the square of the applied bias (V) and inversely by the cube of the film thickness (L) according to eq (2):

$$J = \frac{9}{8}\varepsilon_o \varepsilon_r \mu_h \frac{V^2}{L^3} \qquad (2)$$

Where ε_r is the dielectric permittivity and μ_h is the hole mobility of the active layer. Note that to include the electric field dependency of the mobility, eq 2 can be appropriately modified according to the Mott−Gurney law (eq3):

$$J = \frac{9}{8}\varepsilon_o \varepsilon_r \mu_{h,o} \frac{V^2}{L^3} \exp\left[0.89\beta\left(\frac{V}{L}\right)^{1/2}\right] \qquad (3)$$

where $\mu_h = \mu_{h,o} \exp\left[\beta\left(\frac{V}{L}\right)^{1/2}\right]$ (Poole−Frenkel mobility law), $\mu_{h,0}$ is the zero-field mobility, and β is the field activation factor of the mobility. From Figure 6d, the calculated electron mobilities were 1.92 × 10^{-4} and 4.76 × 10^{-4} cm^2 V^{-1} s^{-1} and 9.77 × 10^{-4} for the devices using the BZO, FTO and BZO:H electrodes, respectively. The enhanced electron mobility and remarkable overall device performance obtained in the device using the hydrogen annealed BZO electrode originates from the formation of a better (Ohmic) contact at the cathode interface and from the reduced electron injection barrier as derived from the electron-only devices analysis.

To gain more insight into the above differences between the devices with the different cathode electrodes we measured their capacitance-voltage (C-V) characteristics in dark (Figure 6 e). C-V measurements in devices based on organic semiconductors are usually exhibiting Mott-Schottky characteristics and can be used to evidence the device built-in field (V_{bi}) which is also related to the presence of charge extraction barriers at electrode contacts. In Figure 6f the Mott-Schottky characteristics of our devices as derived from their C-V measurements are shown, where $C^{-2}=(2/q\varepsilon N)(V_{bi}-V)$, $\varepsilon \approx \varepsilon_o$ is the permittivity of the blend, N is the doping level and q is the elementary charge. Mott-Schottky analysis in Figure 6f allowed us determining the devices built-in field from the intercept of the linear relation with the voltage axis, and simultaneously the doping level from the C^{-2}-V slope. For the devices with the BZO cathode we obtained a V_{bi} of 0.45 V while for the one with the FTO cathode the estimated V_{bi} was 0,44 V. However, the use of BZO:H as the cathode contact delivered an increased V_{bi} of 0.56V. This increase in V_{bi} matches the increase in V_{oc} and indicates that the use of BZO:H cathode electrode induces large strengthening of the device built-in field. This is due to the higher work function difference between both contacts (bottom TCO cathode and MoO_x anode) achieved in the case of low work-function BZO:H.

We also confirmed that the better quality of the cathode contact of our hydrogen annealed BZO-based devices results also in its superior environmental stability as compared to the reference one with the FTO cathode. In Figures 7a, 7b, 7c and 7d the variations of PCE, J_{sc}, V_{oc} and FF of the devices are presented as a function of storage time under ambient conditions. A faster drop in operational characteristics of the reference device was observed, while the device with the BZO:H cathodes exhibits better stability maintaining nearly unaffected its original values, even after storage in air for more than 2500 hours. The slower degradation rate of the latter solar cell may be a result of exceptional environmental stability of the BZO:H layer, as concluded from the stability study presented in Figure S6. It is expected that the device stability and lifetime could be further improved by the use of some more advanced encapsulation technologies for organic solar cells

Finally, in order to demonstrate the universality of our approach we fabricated devices based on the recently introduced small bandgap donor polymers PCDTBT and PTB7. In Figures 8a and 8d the photocurrent and in Figures 8b and 8e the dark current J-V characteristics of PSCs with the structure glass/cathode/ZnO (40 nm)/PCDTBT:$PC_{71}BM$ or PTB7:$PC_{71}BM$ (90 nm)/MoO_x (20 nm) Al, are shown. Results are also summarized in Table 2. The use of BZO:H electrode was proven again beneficial for the device performance. The devices with the BZO anodes and PCDTBT:$PC_{71}BM$ and PTB7:$PC_{71}BM$ active layers gave a PCE of 4.0% and 5.30%, respectively, whereas those with the BZO:H electrodes exhibited high PCE values of 5.90% and 7.25%, respectively, (which were better than the 5.10% and 6.75% obtained in the reference devices with FTO cathodes). Note that, previously a structurally identical PTB7:$PC_{71}BM$-based PSC having an AZO bottom cathode electrode and ZnO and MoO_x electron and hole extraction layers, respectively, yielded an efficiency of 6.15% which was the highest reported for a PSC using a doped ZnO-based transparent electrode, but lower when compared with the 7.25% reported here.[41] Enhanced EQEs (Figures 8c and 8f) and electron currents (Figure S7) were also obtained in the devices with the BZO:H cathodes. The calculated electron mobilities for the measurements taken in PCDTBT:$PC_{71}BM$ based electron only devices were 7.62×10^{-5} cm^2 V^{-1} s^{-1} for the device with the BZO cathode and 2.91×10^{-4} and 7.72×10^{-4} cm^2 V^{-1} s^{-1} for the devices using the FTO and BZO:H electrodes, respectively, whereas the corresponding values obtained in PTB7:$PC_{71}BM$ based electron only devices were 3.12×10^{-5} cm^2 V^{-1} s^{-1} for the device with the BZO cathode and 9.31×10^{-5} and 1.84×10^{-4} cm^2 V^{-1} s^{-1} for the devices with FTO and BZO:H electrodes, respectively. Our findings suggest that in devices with hydrogen annealed BZO used as bottom cathode electrodes substantially improved cathode contacts and enhanced electron mobilities were simoultaneously obtained.

4. Conclusions

In conclusion, we have demonstrated the utility and effectiveness of hydrogen-doped boron-doped ZnO (termed as BZO:H) films which exhibited high conductivity and optical transparency and low work function values for application as bottom cathode electrodes in polymer solar cells using either P3HT:$PC_{71}BM$ or PCDTBT:$PC_{71}BM$ photoactive layers which gave efficiencies of 3.9% and 5.9%, respectively. Those were higher from the corresponding values obtained in the devices using a conventially used FTO cathode. Our findings from the detailed analysis performed in this work provide evidence for the incorporation of hydrogen dopants within the BZO lattice during post-annealing in hydrogen which increases the n-type conductivity of the oxide. Our work demonstrates the first successful implementation of BZO-based transparent conductive oxides as cathode electrode materials in organic optoelectronics. We anticipate that understanding and controlling the electronic and physical properties of electrode materials is a key requirement in order to achieve a major increase in efficiency of polymer solar cells. To this end, the ability to control the electrical, optical and electronic properties of ZnO-based TCOs via hydrogen doping will spur progress in the development of ITO-free organic optoelectronic devices.

Supporting Information

Additional Figures and text are included in SI (Figures S1-S7).

Acknowledgements

The project “Implementing advanced interfacial engineering strategies for highly efficient hybrid solar cells” (Acronym: IMAGINE-HYSOL) is implemented under the "ARISTEIA II" Action of the OPERATIONAL PROGRAMME EDUCATION AND LIFELONG LEARNING" and is co-funded by the European Social Fund (ESF) and National Resources.

References

1. G. Yu, J. Gao, J. C. Hummelen, F. Wudl and A. J. Heeger, *Science*, 1995, **270**, 1789-1791.
2. M. A Green, K. Emery, Y. Hishikawa, W. Warta and E. D. Dunlop, *Prog. Photovolt. Res. Appl.*, 2013, **20**, 12-20.
3. S. Mathew, A. Yella, P. Gao, R. Humphry-Baker, B. F. E. Curchod, N. Ashari-Astani, I. Tavernelli, U. Rothlisberger, Md. K. Nazeeruddin and M. Grätzel, *Nat. Chem.*, 2014, **6**, 242-247.
4. N. K. Noel, S. D. Stranks, A. Abate, C. Wehrenfennig, S. Guarnera, A. Haghighirad, A. Sadhanala, G. E Eperon, S. K. Pathak, M. B Johnston, L. Herz and H. Snaith, ***Energy Environ. Sci.***, 2014, **7**, 3061-3068.
5. S.-H. Liao, H.-J. Jhuo, P.-N. Yeh, Y.-S. Cheng, Y.-L. Li, Y.-H. Lee, S. Sharma and S.-A. Chen, *Sci. Rep.*, 2014, ***4***, 6813.
6. Y. Liu, J. Zhao, Z. Li, C. Mu, W. Ma, H. Hu, K. Jiang, H. Lin, H. Ade and H. Yan, *Nat.Comm.*, 2014, **5**, 5293.
7. Z. He, B. Xiao, F. Liu, H. Wu, Y. Yang, S. Xiao, C. Wang, T. P. Russell and Y. Cao., *Nature Photon.*, 2015, **9**, 174-179.
8. J.-D. Chen, C. Cui, Y.-Q. Li, L. Zhou, Q.-D. Ou, C. Li, Y. Li and J.-X. Tang, *Adv. Mater.*, 2015, **27**, 1035-1041.
9. J. You, L. Dou, K. Yoshimura, T. Kato, K. Ohya, T. Moriarty, K. Emery, C.-C. Chen, J. Gao, G. Li and Y. Yang, *Nat. Comm.*, 2013, **4**, 1446.
10. J. You, C.-C. Chen, Z. Hong, K. Yoshimura, K. Ohya, R. Xu, S. Ye, J. Gao, G. Li and Y. Yang, *Adv. Mater.*, 2013, **25**, 3973-3978.
11. Y. Liu, C.-C. Chen, Z. Hong, J. Gao, Y. M. Yang, H. Zhou, L. Dou, G. Li and Y. Yang, *Sci. Rep.*, 2013, **3**, 3356.
12. C.-C. Chen, W.-H. Chang, K. Yoshimura, K. Ohya, J. You, J. Gao, Z. Hong and Y. Yang, *Adv. Mater.*, 2014, **26**, 5670-5677.
13. Y. Li, *Acc. Chem. Res.*, 2012, **45**,723-733.

14. C. Duan, F. Huang and Y. Cao, *J. Mater. Chem.*, 2012, **22**, 10416-10434.
15. L.-M. Chen, Z. Xu, Z. Hong and Y. Yang, *J. Mater. Chem.*, 2010, **20**, 2575-2598.
16. H.-L. Yip and A. K.-Y. Jen, *Energy Environ. Sci.*, 2012, **5**, 5994-6011.
17. C. K. Song, A. C. White, L. Zeng, B. J. Leever, M. D. Clark, J. D. Emery, S. J. Lou, A. Timalsina, L. X. Chen, M. J. Bedzyk and T. J. Marks, *ACS Appl. Mater. Interfaces*, 2013, **5**, 9224-9240.
18. A. Stadler, *Materials*, 2012, **5**, 661-683.
19. Y.-S. Shim, H. G. Moon, D. H. Kim, H. W. Jang, C.-Y. Kang, Y. S. Yoon and S.-J. Yoon, *Sens. Actuator B-Chem.*, 2011, **160**, 357-363.
20. S. Calnan, *Coatings*, 2014, **4**, 162-202.
21. Y. Liu, Y. Li and H. Zeng, *J. Nanomater.*, 2013, **2013**, 196521.
22. B. N. Pawar, G. Cai, D. Ham, R. S. Mane, T. Ganesh, A. Ghule, R. Sharma, K. D. Jadhava and S.-H. Han, *Sol. Energy. Mat. Sol. Cells*, 2009, **93**, 524-527.
23. W.-L. Lu, P.-K. Hung, C.-I. Hung, C.-H. Yeh and M.-P. Houng, *Mater. Chem. Phys.*, 2011, **130**, 619-623.
24. L. Zhu, J. Li, Z. Ye, H. He, X. Chen and B. Zhao, *Opt. Mater.*, 2008, **31**, 237-240.
25. R. Biswal, A. Maldonado, J. Vega-Pérez, D. R. Acosta and M. De La Luz Olvera, *Materials*, 2014, **7** 5038-5046.
26. F.-C. Chiu, *Materials*, 2014, **7**, 7339-7348.
27. D. Lincot, *MRS Bull.*, 2010, **35**, 778-789.
28. Ü. Özgür, Ya. I. Alivov, C. Liu, A. Teke, M. A. Reshchiko, S. Doğan, V. Avrutin, S.-J. Cho and H. Morkoç, *J. Appl. Phys.*, 2005, **98**, 041301.
29. Z. R. Tian, J. A. Voigt, J. Liu, B. Mckenzie, M. J. Mcdermott, M. A. Rodriguez, H. Konishi and H. Xu, *Nat. Mater.*, 2003, **2**, 821-826.
30. M. Law, L. E. Greene, J. C. Johnson, R. Saykally and P. Yang, *Nat. Mater.*, 2005, **4**, 455-459.
31. Z. Yin, Q. Zheng, S.-C. Chen, D. Cai, L. Zhou and J. Zhang, *Adv. Energy Mater.*, 2014, **4**, 1301404.

32. J. Y. Kim, E. Cho, J. Kim, H. Shin, J. Roh, M. Thambidurai, C.-m. Kang, H.-J. Song, S. M. Kim, H. Kim and C. Lee, *Opt. Express*, 2015, **23**, A1334-A1341.
33. N. Zhou, M.-G. Kim, S. Loser, J. Smith, H. Yoshida, X. Guo, C. Song, H. Jin, Z. Chen, S. M. Yoon, A. J. Freeman, R. P. H. Chang, A. Facchetti and T. J. Marks, *Proc. Natl. Acad. Sci. U S A.*, **112**, 7897-902.
34. Z. Hu, J. Zhang and Y. Zhu, *Sol. Energ. Mater. Sol. Cells*, 2013, **117**, 610-616.
35. M. Thambidurai, J. Y. Kim, C.-m. Kang, N. Muthukumarasamy, H.-J. Song, J. Song, Y. Ko and D. Velauthapillai, C. Lee, *Renew. Energy*, 2014, **66**, 433-442.
36. H. Oh, J. Krantz, I. Litzov, T. Stubhan, L. Pinna and C. J. Brabec, *Sol. Energy Mater. Sol. Cells*, 2011, **95**, 2194-2199.
37. K.-S. Shin, K.-H. Lee, H. H. Lee, D. Choi and S.-W. Kim, *J. Phys. Chem. C*, 2010, **114**, 15782-15785.
38. T. Stubhan, I. Litzov, N. Li, M. Salinas, M. Steidl, G. Sauer, K. Forberich, G. J. Matt, M. Halik and C. J. Brabec, *J. Mater. Chem. A*, 2013, **1**, 6004-6009.
39. M. Thambidurai, J. Y. Kim, J. Song, Y. Koa, N. Muthukumarasamy, D. Velauthapillai and C. Lee, *Sol. Energy*, 2014, **106**, 95-101.
40. S. Trost, K. Zilberberg, A. Behrendt, A. Polywka, P. Görrn, P. Reckers, J. Maibach, T. Mayer and T. Riedl, *Adv. Energy Mater.*, 2013, **3**, 1437-1444.
41. H. Liu, Z. Wu, J. Hu, Q. Song, B. Wu, H. L. Tam, Q. Yang, W. H. Choi and F. Zhu, *Appl. Phys. Lett.*, 2013, **103**, 043309.
42. D. Chen, C. Zhang, Z. Wang, J. Zhang, S. Tang, W. Wei, L. Sun and Y. Hao, *Appl. Phys. Lett.*, 2014, **104**, 243301.
43. J. Owen, M. S. Son, K.-H. Yoo, B. D. Ahn, and S. Y. Lee, *Appl. Phys. Lett.*, 2007, **90**, 033512.
44. G. B. Murdoch, S. Hinds, E. H. Sargent, S. W. Tsang, L. Mordoukhovski and Z. H. Lu, *Appl. Phys. Lett.*, 2009, **94**, 213301.
45. J. H. Park, K. J. Ahn, K. I. Park, S. I. Na and H. K. Kim, *J. Phys. D: Appl. Phys.*, 2010, **43**, 115101.

46. H.-K. Park, J.-W. Kang, S.-I. Na, D.-Y. Kim and H.-K. Kim, *Sol. Energy Mater. Sol. Cells*, 2009, **93**, 1994-2002.
47. D. S. Ghosh, T. L. Chen, N. Formicaa, J. Hwangb, I. Bruderb and V. Pruneria, *Sol. Energy Mater. Sol. Cells*, 2012, **107**, 338-343.
48. A. D. Sio, K. Chakang, O. Sergeev, K. von Maydell, J. Parisi and E. von Hauff, *Sol. Energy Mater. Sol. Cells*, 2012, **98**, 52-56.
49. V. Bhosle, J. T. Prater, Fan Yang, D. Burk, S. R. Forrest and J. Narayan, *J. Appl. Phys.*, 2007, **102**, 023501.
50. A. Soultati, A. M. Douvas, D. G. Georgiadou, L. C. Palilis, T. Bein, J. M. Feckl, S. Gardelis, M.Fakis, S. Kennou, P. Falaras, T. Stergiopoulos, N. A. Stathopoulos, D. Davazoglou, P. Argitis and M.Vasilopoulou, *Adv. Energy Mater.*, 2014, **4**, 1300896.
51. A. M. Douvas, M. Vasilopoulou, D. G. Georgiadou, A. Soultati, D. Davazoglou, N. Vourdas, K. P. Giannakopoulos, A. G. Kontos, S. Kennou and P. Argitis, *J. Mater. Chem. A*, 2014, **2**, 6290-6300.
52. C. G. Van de Walle, *Phys. Rev. Lett.*, 2000, **85**, 1012-1015.
53. C. G. Van de Walle and J. Neugebauer, *Nature (London)*, 2003, **423**, 626-628.
54. S. F. J. Cox, E. A. Davis, S. P. Cottrell, P. J. C. King, J. S. Lord, J. M. Gil, H. V. Alberto, R. C. Vilão, J. Poroto Duarte, N. Ayres de Campos, A. Weidinger, R. L. Lichti and S. J. C. Irvine, *Phys. Rev. Lett.*, 2001, **86**, 2601-2604.
55. Ü. Özgür, A. Teke, C. Liu, S.-J. Cho, H. Morkoc, O. Everitt, *Appl. Phys. Lett.*, 2004, **84**, 3223-3225.
56. T. Koida, S. F. Chichibu, A. Uedono, A. Tsukazaki, M. Kawasaki, T. Sota, Y. Segawa and H. Koinuma, *Appl. Phys. Lett.*, 2003, **82**, 532-534.
57. N. Y. Lee, K.-J. Lee, C. Lee, J.-E. Kim, H. Y. Park, D.-H. Kwak, H.-C. Lee and H. Lim, *J. Appl. Phys.*, 1995, **78**, 3367-3370.
58. B. D. Cullity and S. R. Stock, *Elements of XRD*, Prentice Hall, 2001, 167-171.
59. O. Lupan, T. Pauporté, L. Chow, B. Viana, F. Pellé, L.K. Ono, B. Roldan Cuenya and H. Heinrich, *Appl. Surf. Sci.*, 2010, **256**, 1895–1907.
60. J. Cho, K.-H. Yoon, M.-S. Oh, W.-K. Choi, *J. Electrochem. Soc.*, 2003, **150**, H225-H228.

61. H. Ishizaki, M. Imaizumi, S. Matsuda, M. Izaki and T. Ito, *Thin Solid Films*, 2002, **411**, 65–68.

62. E. C. Onyiriuka, *J. Non-Cryst. Solids*, 1993, **163**, 268–273.

63. M. Kröger , S. Hamwi , J. Meyer , T. Riedl , W. Kowalsky and A. Kahn, *Org. Electron.*, 2009, **10**, 932-938.

64. M. T. Greiner, M. G. Helander, W.-M. Tang, Z.-B. Wang, J. Qiu and Z.-H. Lu, *Nat. Mater.*, 2012, **11**, 76-81.

65. Z. He, C. Zhong, X. Huang, W.-Y. Wong, H. Wu, L. Chen, S. Su and Y. Cao, *Adv. Mater.*, 2011, **23**, 4636-4643.

66. P. P. Boix, G. Garcia-Belmonte, U. Munecas, M. Neophytou, C. Waldauf and R. Pacios, *Appl. Phys. Lett.*, 2009, **95**, 233302.

67. Z. He, C. Zhong, X. Huang, W.-Y. Wong, H. B. Wu, L. Chen, S. J. Su and Y. Cao, *Adv. Mater.*, 2011, **23**, 4636-4643.

Figures captions

Figure 1 Dependence of (a) resistivity (squares) and carrier concentration (circles), (b) Hall mobility (triangles) and sheet resistance (rhombus) on the boron content of BZO films. Variation of (c) resistivity and carrier concentration, (d) Hall mobility and sheet resistance on the hydrogen annealing temperature of BZO:H films.

Figure 2 (a) Room temperature PL spectra of BZO and BZO:H films. (b) Time-resolved PL responses of the same films. (c) Optical transmittance spectra of BZO and BZO:H film and (d) the tauc plots for the determination of the optical bandgap of both films.

Figure 3 X-ray diffraction pattern of 100 nm (a) as-deposited and (b) hydrogen-doped BZO films. Scanning electron microscopy topographies of 100 nm (c) BZO and (d) BZO:H films.

Figure 4 (a) XPS core level peaks of BZO and BZO:H films: (a) Zn 2p, (b) B 1s and (c) O 1s peaks. (d) The secondary electron cut-off and (e) valence band derived from UPS measurements in BZO, BZO:H and FTO films.

Figure 5 (a) The architecture of the inverted devices using different bottom cathode electrode and the chemical structures of organic semiconductors used in this study. (b) and (c) The energy level alignment (before contact) between different layers used in these devices in the cases of FTO and BZO:H cathode electrodes, respectively.

Figure 6 (a) J-V curves for P3HT:$PC_{71}BM$ based PSCs using different bottom electrodes under AM1.5 illumination. (b) Dark J-V characteristics, and (c) EQEs of the same devices. (d) J-V curves of electron only devices. (e) C-V and (f) Mott-Schottky characteristics of the same devices.

Figure 7 Variation with time of (a) PCE, (b) J_{sc}, (c)V_{oc} and (d) FF of the inverted P3HT:$PC_{71}BM$-based cells stored for 5000 hours in air under ambient conditions.

Figure 8 (a) J-V characteristics for PCDTBT:$PC_{71}BM$ based PSCs using different bottom cathode electrodes under AM1.5 illumination. (b) Dark J-V characteristics, and (c) EQEs of the same devices. (d) and (e) Photo and dark J-V characteristic curves and (f) EQEs of PTB7:$PC_{71}BM$ based devices using different bottom cathode layers.

Tables

Table 1. Device characteristics of PSCs having the device configuration BZO or BZO:H or FTO/ZnO/P3HT:$PC_{71}BM/MoO_x$/Al (mean values and standard deviations were extracted from a batch of 24 devices).

PSC 1 **(P3HT:$PC_{71}BM$)**				
Anode	**J_{sc} (mA/cm^2)**	**V_{oc} (V)**	**FF**	**PCE (%)**
BZO	8.2(±0.25)	0.59(±0.02)	0.59(±0.02)	2.8(±0.15)
BZO:H	10.3(±0.15)	0.62(±0.01)	0.60(±0.01)	3.9(±0.15)
FTO	9.5(±0.15)	0.57(±0.01)	0.60(±0.01)	3.3(±0.10)

Table 2. Device characteristics of PSCs having the device configuration BZO or BZO:H or FTO/ZnO/ PCDTBT:$PC_{71}BM$ or PTB7:$PC_{71}BM/MoO_x$/Al (mean values and standard deviations were extracted from a batch of 24 devices).

PSC 2 **(PCDTB:$PC_{71}BM$)**				
Anode	**J_{sc}(mA/cm^2)**	**V_{oc} (V)**	**FF**	**PCE (%)**
BZO	7.9(±0.30)	0.85(±0.20)	0.60(±0.20)	4.0(±0.25)
BZO:H	10.8(±0.20)	0.88(±0.10)	0.62(±0.10)	5.9(±0.20)
FTO	9.7(±0.15)	0.84(±0.10)	0.62(±0.10)	5.1(±0.15)

PSC 3 **(PTB7:$PC_{71}BM$)**				
Anode	**J_{sc}(mA/cm^2)**	**V_{oc} (V)**	**FF**	**PCE (%)**
BZO	10.90 (±0.15)	0.72 (±0.01)	0.68 (±0.01)	5.30 (±0.25)
BZO:H	14.00 (±0.10)	0.74 (±0.01)	0.70 (±0.01)	7.25 (±0.25)
FTO	13.70 (±0.10)	0.70 (±0.01)	0.70 (±0.01)	6.75 (±0.25)

Figures

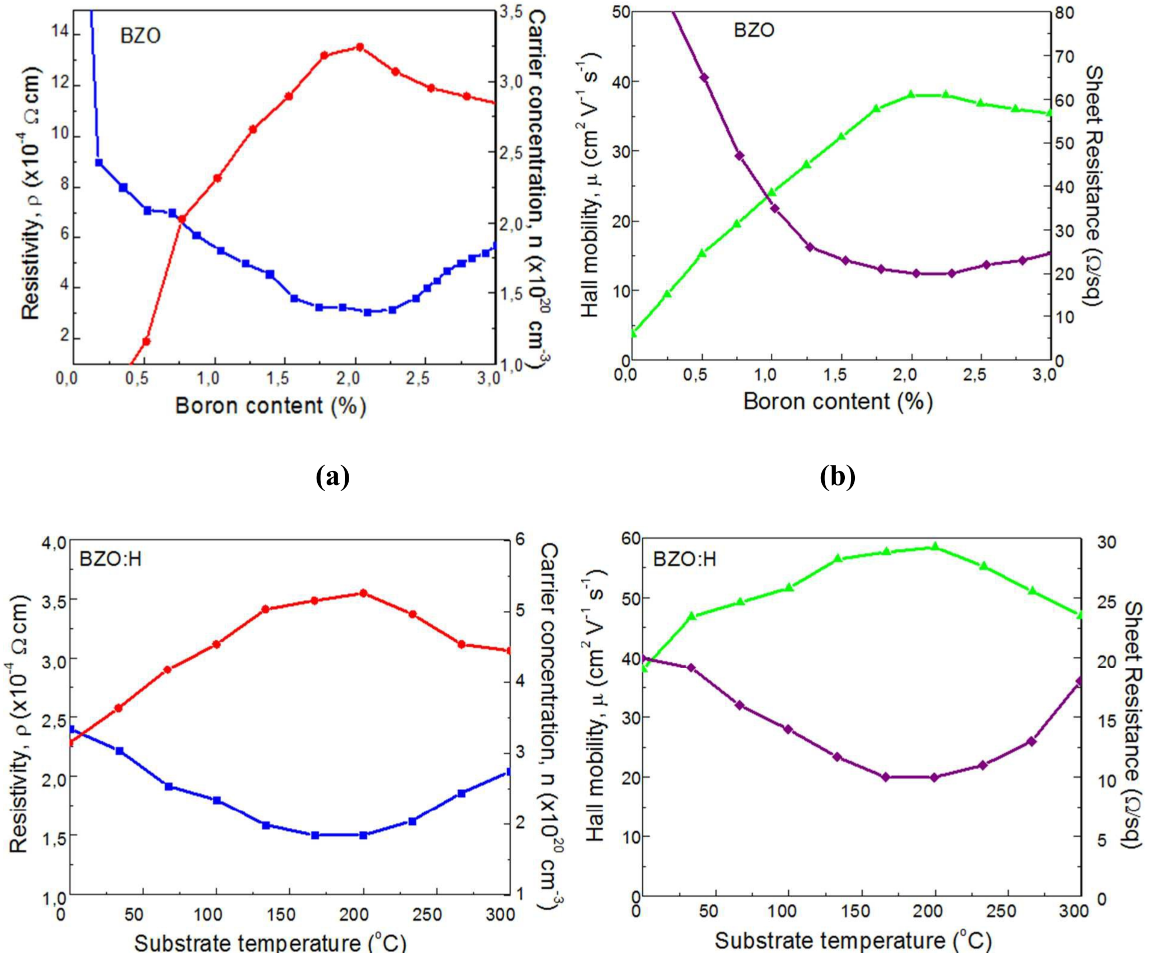

(a) (b)

(c) (d)

Figure 1

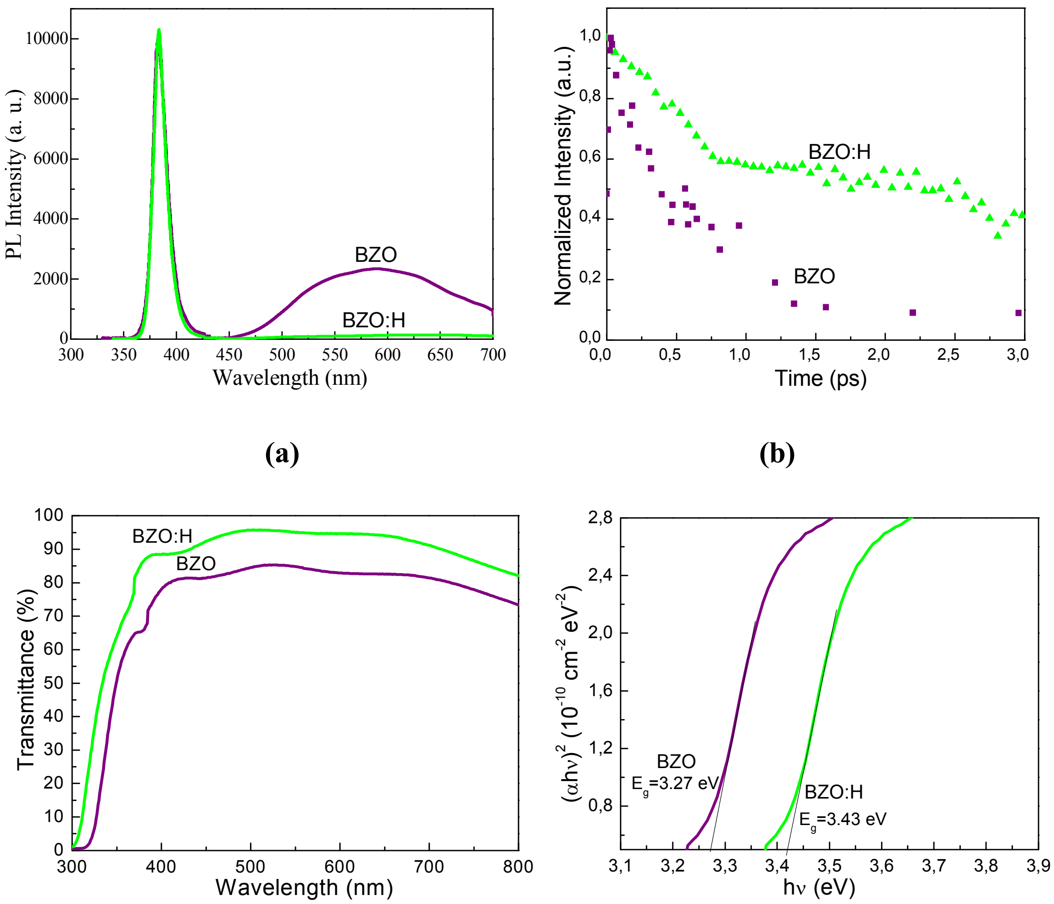

(a) **(b)**

(c) **(d)**

Figure 2

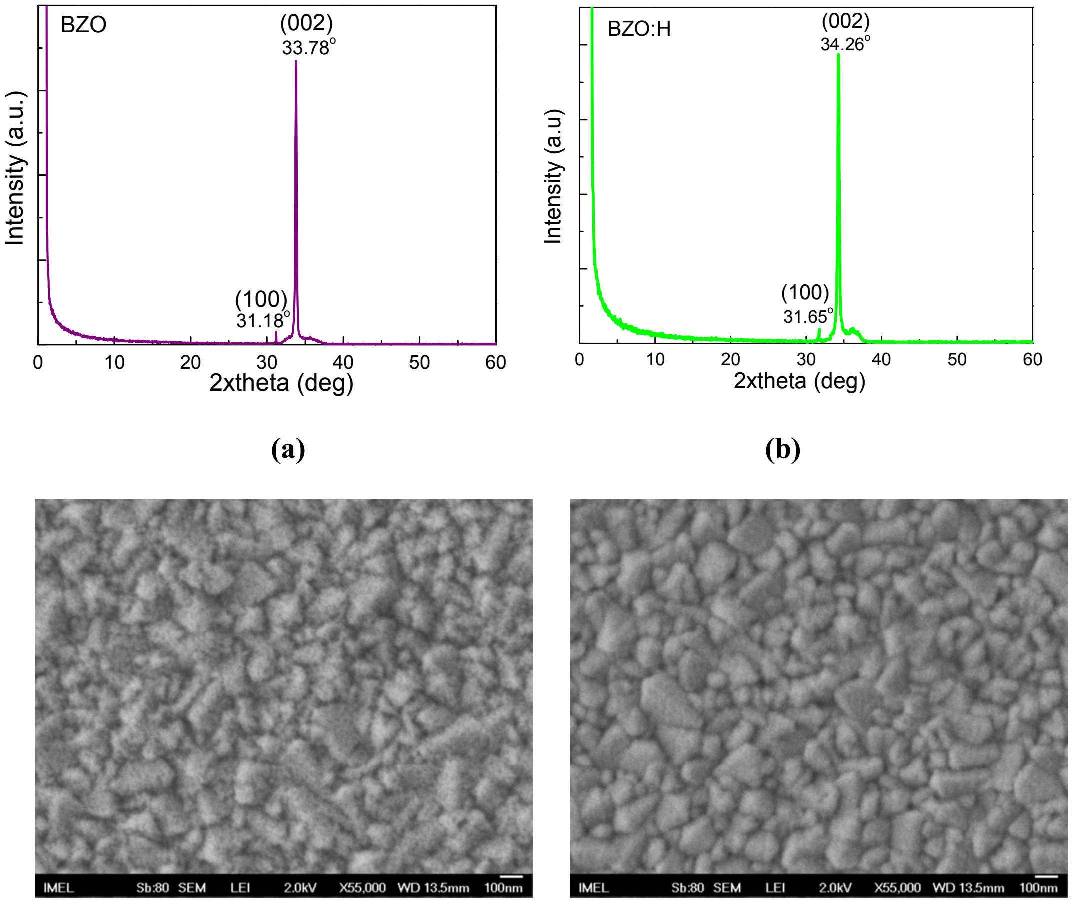

(a) (b)

(c) (d)

Figure 3

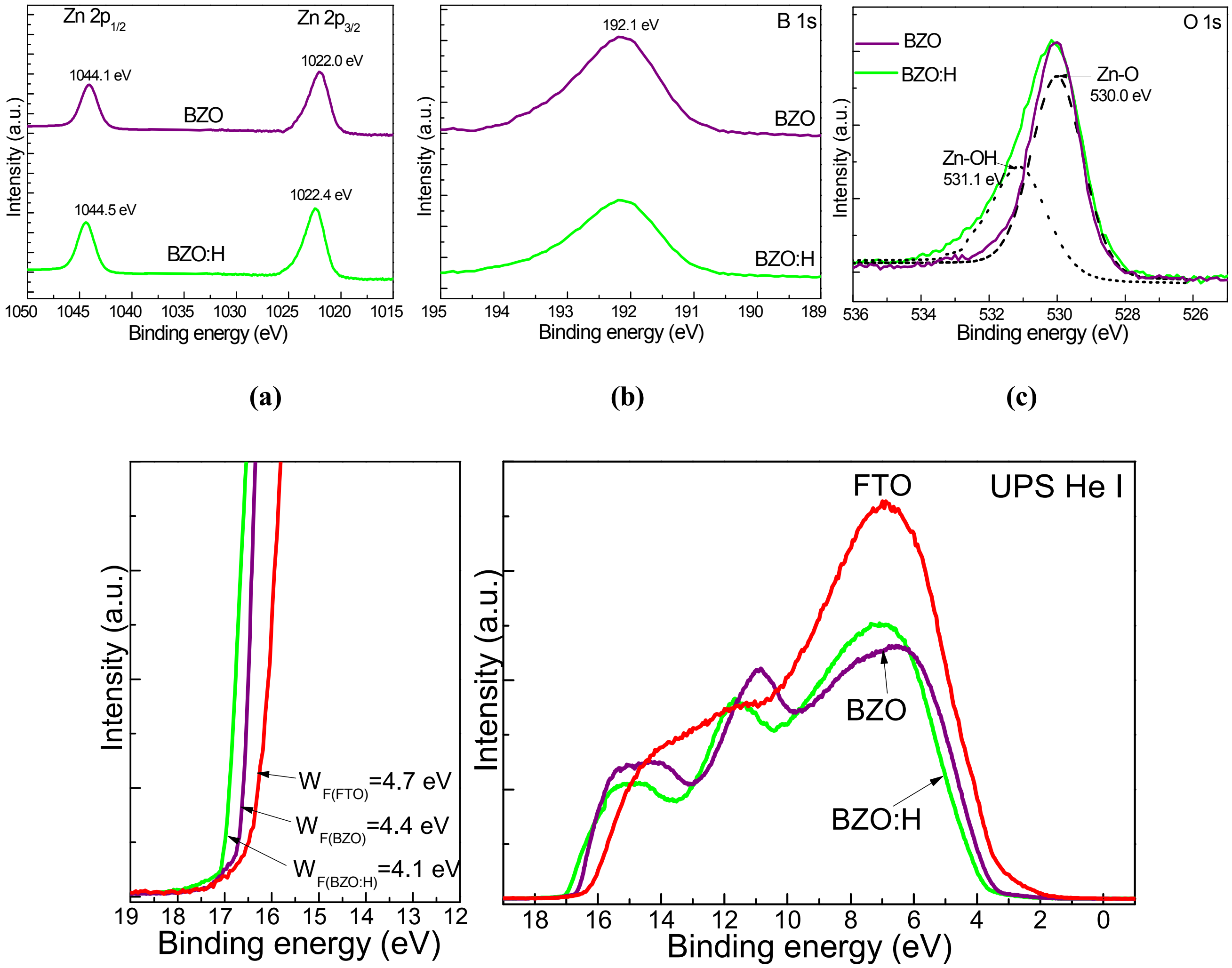

(a) (b) (c)

(d) (e)

Figure 4

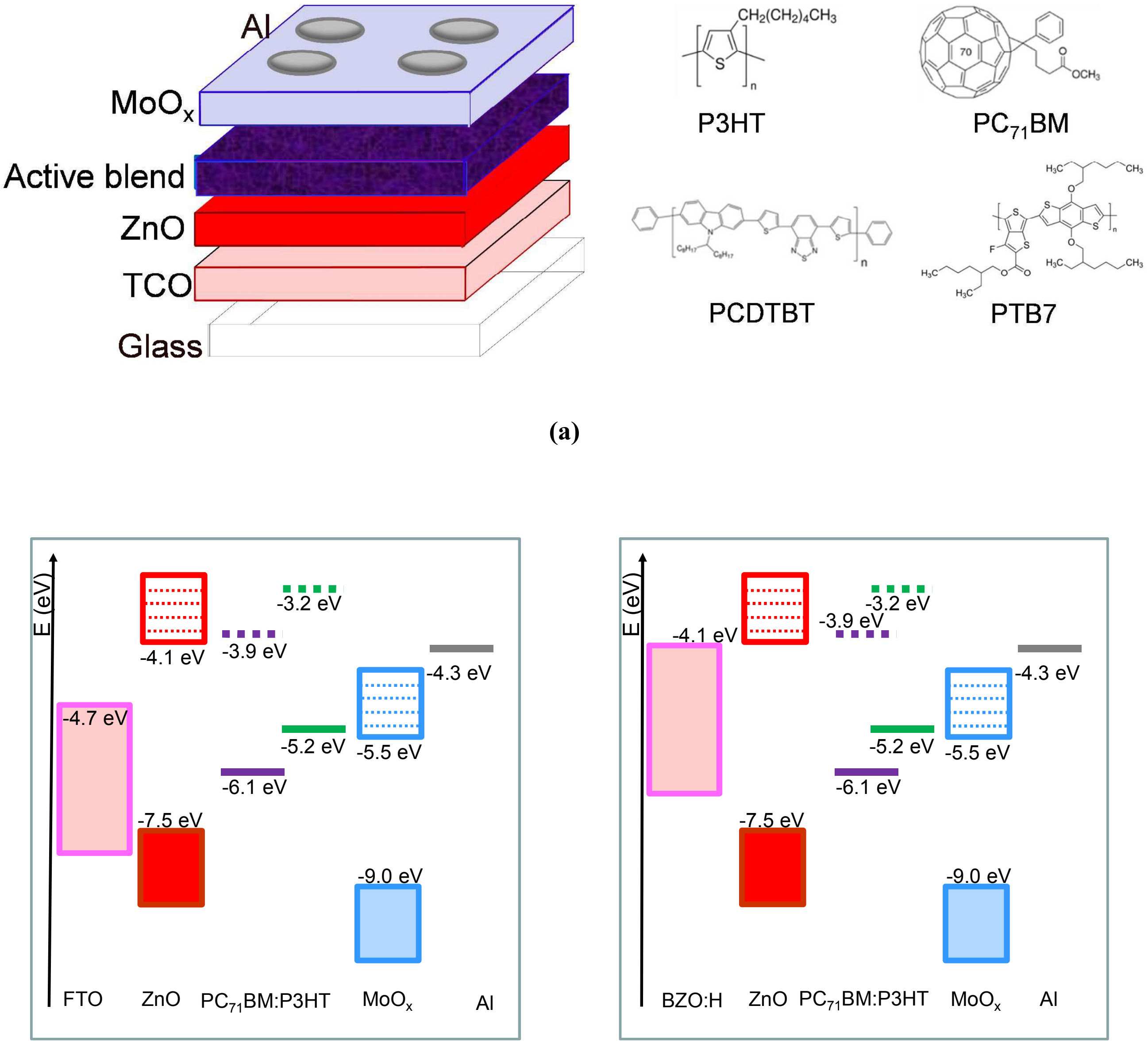
Al
MoOx
Active blend
ZnO
TCO
Glass
CH2(CH2)4CH3
S
n
P3HT
70
OCH3
PC71BM
N
C8H17
C8H17
N S N
n
PCDTBT
H3C
CH3
O
S
F
H3C
CH3
H3C
PTB7
E (eV)
-4.7 eV
-4.1 eV
-7.5 eV
-3.9 eV
-6.1 eV
-3.2 eV
-5.2 eV
-5.5 eV
-9.0 eV
-4.3 eV
FTO
ZnO
PC71BM:P3HT
MoOx
Al
E (eV)
-4.1 eV
-7.5 eV
-3.9 eV
-3.2 eV
-5.2 eV
-6.1 eV
-5.5 eV
-9.0 eV
-4.3 eV
BZO:H
ZnO
PC71BM:P3HT
MoOx
Al

(a)

(b) (c)

Figure 5

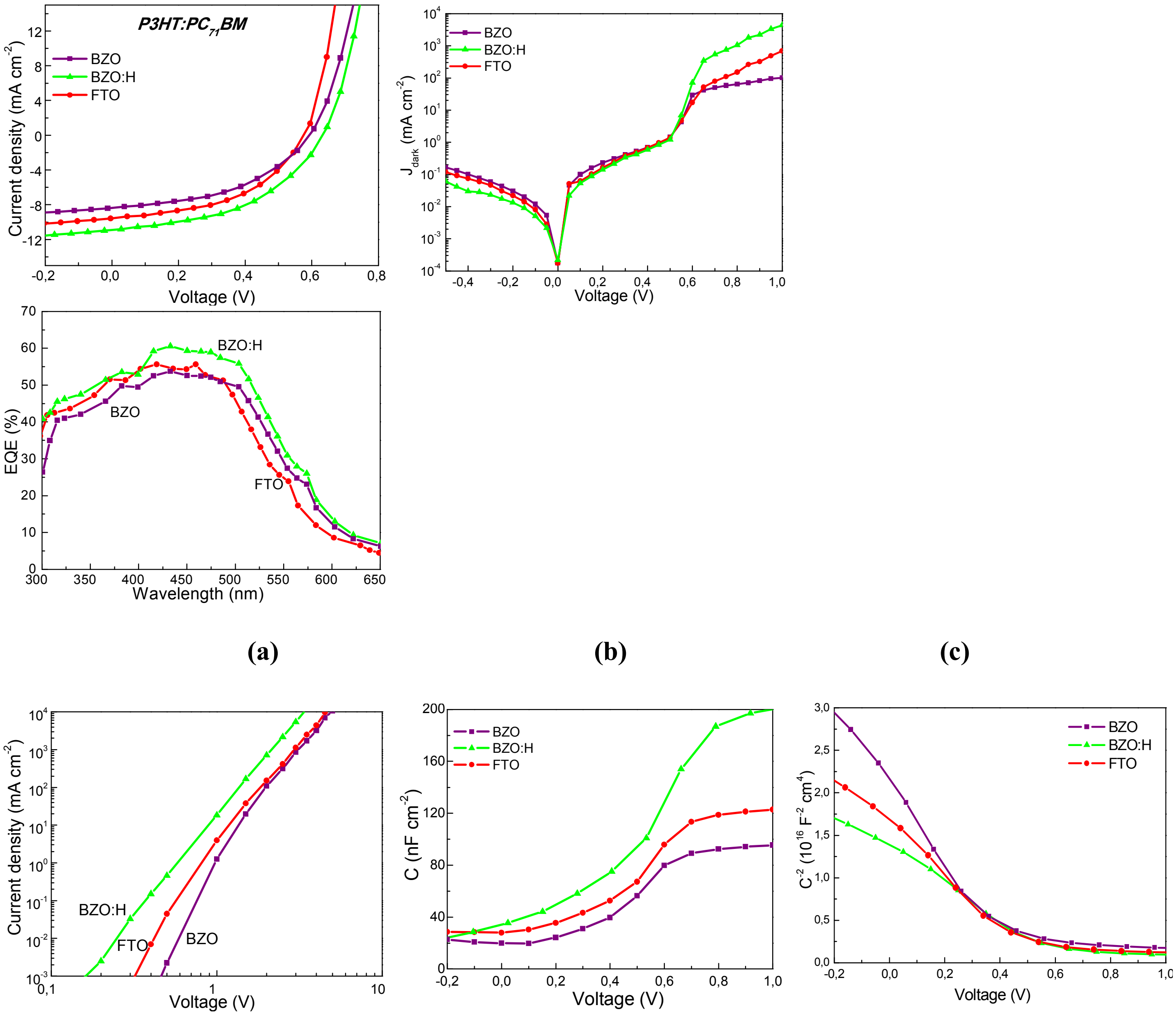

(a) **(b)** **(c)**

(d) **(e)** **(f)**

Figure 6

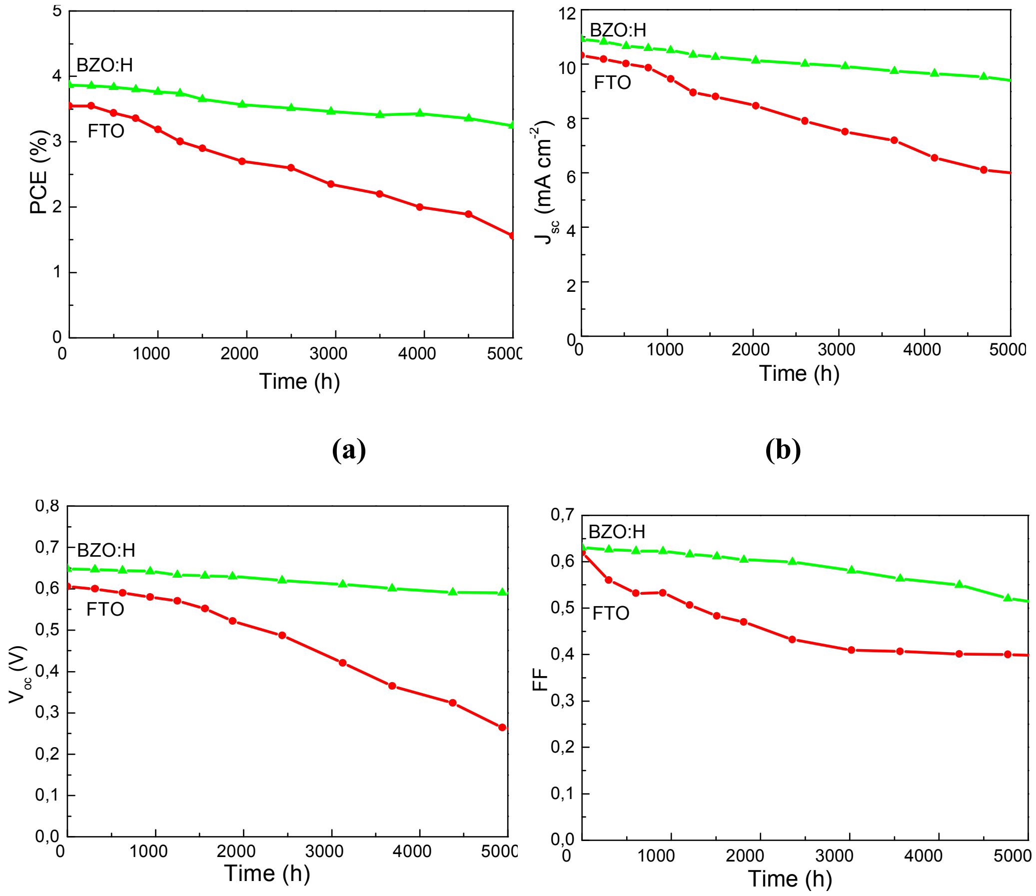

(a) **(b)**

(c) **(d)**

Figure 7

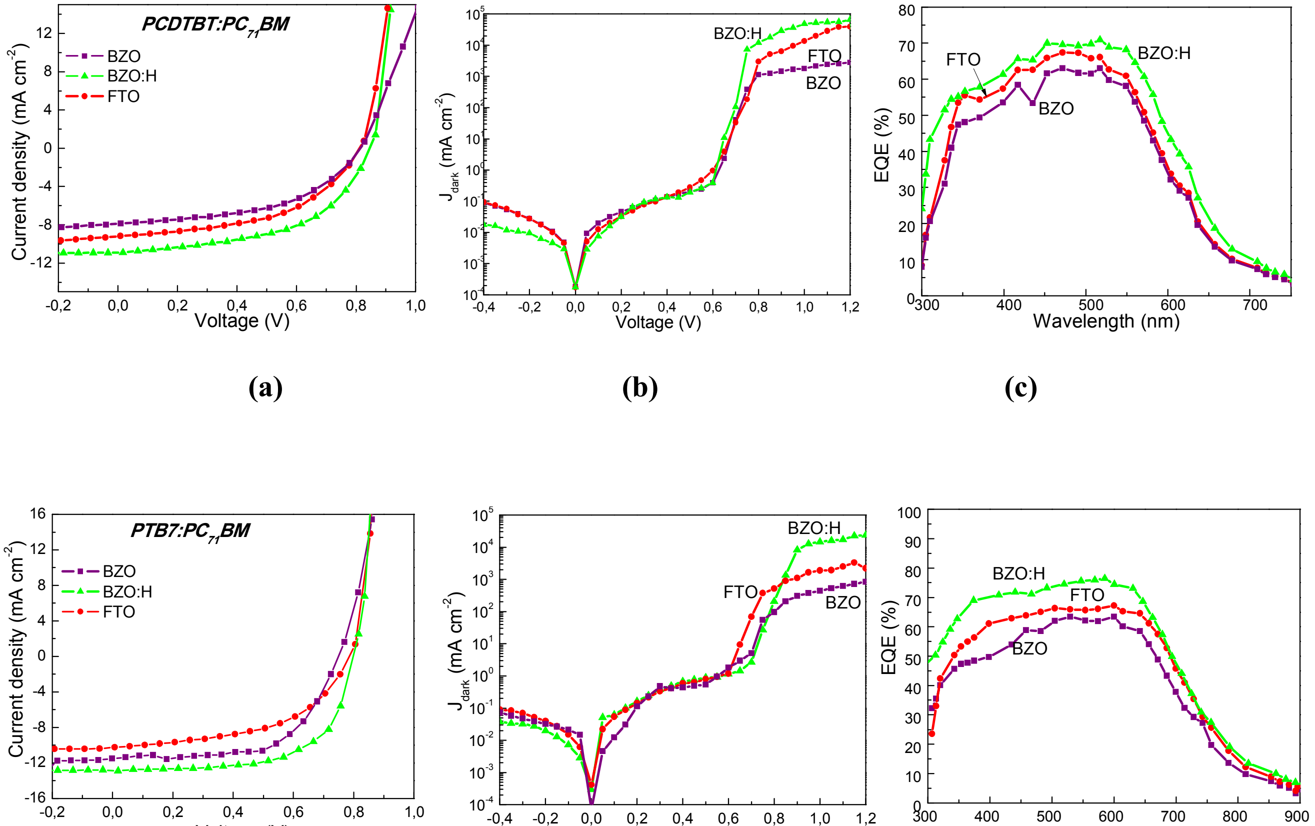

(a) (b) (c)

(d) (e) (f)

Figure 8

Table of Contents (TOC)

Here the benefits of hydrogen-doped boron-doped ZnO layers for use as efficient bottom cathode electrodes in polymer solar cells are explored.